Emission, transport and radiative effects of mineral dust from Taklimakan and Gobi Deserts: comparison of measurements and model results

Siyu Chen[1], Jianping Huang[1*], Litai Kang[1], Hao Wang[1], Xiaojun Ma[1], Yongli He[1], Tiangang Yuan[1], Ben Yang[2], Zhongwei Huang[1], and Guolong Zhang[1]

[1] Key Laboratory for Semi-Arid Climate Change of the Ministry of Education, Lanzhou University, Lanzhou, China

[2] School of Atmospheric Sciences, Nanjing University, Nanjing, China

Manuscript for submission to ACP

*Corresponding author: Jianping Huang; phone: 0931-8914139;

Email: hjp@lzu.edu.cn

Abstract

The weather research and forecasting model with chemistry (WRF-Chem) was used to investigate a typical dust storm event that occurred from 18th to 23rd March 2010 and swept across almost all of China, Japan, and Korea. The spatial and temporal variations in dust aerosols and the meteorological conditions over East Asia were well reproduced in WRF-Chem model. The simulation results were used to further investigate details of processes related to dust emission, long-range transport, and radiative effects of dust aerosols over the Taklimakan desert (TD) and Gobi desert (GD). The results showed that weather conditions, topography and surface types in dust source regions may influence dust emission, uplift height and transport at regional scale. The GD was located in the warm zone in advance of the cold front in this case. Rapidly warming surface temperatures and cold air advection at high levels caused strong instability in the atmosphere which strengthened the downward momentum transported from the middle and low troposphere and caused strong surface winds. Moreover, the GD is located in relatively flat, high altitude regions influenced by the confluence of the northern and southern westerly jets. Therefore, the GD dust particles were easily lofted to 4 km and were the primary contributor to the dust concentration over East Asia. In the dust budget analysis, the dust emission flux over the TD was 27.2±4.1 μg m^{-2} s^{-1}, which was similar to that over the GD (29±3.6 μg m^{-2} s^{-1}). However, the transport contribution of the TD dust (up to 0.8 ton day^{-1}) to the dust sink was much smaller than that of the GD dust (up to 3.7 ton day^{-1}) because of the complex terrain and the prevailing wind in the TD. It is noted that a small amount of the TD dust ($PM_{2.5}$ dust concentration was approximately 8.7 ug m^{-3}) was lofted to more than 5 km and transported over greater distances under the influence of the westerly jets. Moreover, the direct radiative

forcing induced by dust was estimated as -3 W m^{-2} and -7 W m^{-2} at the top of the atmosphere, -8 W m^{-2} and -10 W m^{-2} at the surface, and +5 W m^{-2} and +3 W m^{-2} in the atmosphere over the TD and GD, respectively. The study provided confidence for further understanding the climate effects of the GD dust.

Key words: East Asian dust, Dust modelling, WRF-Chem model, Taklimakan desert, and Gobi desert

1. Introduction

Dust is regarded as a major component of tropospheric aerosols in the global atmosphere [Forster et al., 2007; Zhang et al., 2003; Bi et al., 2011]. It is considered to have a significant direct effect on climate by altering the radiative balance between the incoming solar and outgoing planetary radiation in the atmosphere [Ramanathan et al., 2001; Huang et al., 2008a, b, c, 2009, 2010, 2011; Fu et al., 2009; Han et al., 2012; Zhao et al., 2013; Chen et al., 2014b]. In addition, dust can also indirectly modify the microphysical properties of clouds by influencing cloud condensation nuclei and ice cores and thus influence precipitation efficiency [Koren et al., 2004; Huang et al., 2006a, b, c, 2010, and 2014; Su et al., 2008; Qian et al., 2009; Li et al., 2010]. Therefore, dust aerosols have important roles in changing the energy budget and atmospheric and hydrological system at regional and even global scales [Wang et al., 2010; Wang et al., 2012; Huang et al., 2010, 2014; Li et al., 2011; Zhao et al., 2011, 2012].

East Asian dust is entrained from China and its surrounding regions, which constitute the second largest contributor to global dust aerosols [Rea, 1994; Zhang et al., 2003; Ye et al., 2012]. The Taklimakan desert (TD) and Gobi desert (GD) are regarded as two major dust source regions in East Asia (Fig. 1a) [Sun et al., 2001]. The TD is the location of the second largest shifting sand desert in the world and covers an area of 337,000 km^2, approximately 85% of which is covered by shifting sand dunes [Ge et al., 2014]. It is located in the Tarim Basin and is surrounded by the Kunlun Shan Mountains (average elevation 5.5 km) to the south, the Tianshan Mountains (average elevation 4.8 km) to the north and the Pamir Plateau (average elevation 5.5 km) to the west. The GD covers parts of northern China, northwestern China, and southern Mongolia, which is bounded by the TD in the west, the North China Plain in the southeast, and the Hexi Corridor and Tibetan Plateau in the southwest.

Airborne dust over the TD may play an important role in the global radiative energy budget [Huang et al., 2009, 2015]. Special efforts have been dedicated to understanding the spatial and temporal features of the TD dust [Liu et al., 2016], including dust emission [Zhang et al., 2003; Zhao et al., 2003, 2006a; Shao et al., 2011; Chen et al., 2013, 2014a; Xiong et al., 2013], long-range transport [Uno et al., 2001; Han et al., 2005, 2006, 2008; Zhao et al., 2006b, 2007; Huang et al., 2007], dust radiative forcing [Takamura et al.,2004, 2005; Su et al., 2008; Huang et al., 2009; Ye et al., 2012], and its climatic effects [Huang et al., 2006a, b, 2007, 2010 ,2014] over the TD. However, few of these studies have investigated the role of GD dust in the earth-atmosphere system, especially concerning the differences and similarities of dust emission and transport over the GD and TD. Using dust storm reports of 1960-1999, Sun et al. (2001) have found that the GD is the dominant dust source region for East Asia. The dust deposited over East Asia including the Loess Plateau in China and offshore regions. Using Cloud-Aerosol Lidar and Infrared Pathfinder Satellite Observation (CALIPSO) and surface measurements, Huang et al. (2008) have found that dust events are more frequent over the TD, where suspended dust was dominant locally, whereas GD dust storms were less frequent but more intensive. Zhang et al. (2008) have showed that the GD accounted for more than 75% of the dust emission events in all of East Asia using time-series of Multi-angle Imaging SpectroRadiometer (MISR) images. However, it is difficult to use observational data to quantify the details of TD and GD dust emission fluxes and to distinguish the contributions of the TD and GD to dust transport in the downwind deposition regions of East Asia.

In this study we focused on a state-of-the-art model that simulates detailed dust processes to investigate a typical dust event over East Asia that occurred on 18^{th}-23^{rd} March 2010. This dust storm is the strongest since 2006, in terms of scope, intensity and duration of activities. It swept across almost 21 provinces in China, covering an area of 282×104 km^2 and affected about 2.7×10^8 people. Dust particles have even been long-range transported to Shenzhen, Hong Kong and Taiwan. Due to its strong influence, Hong Kong reported an air pollution index exceeded 400 and Shen Zhen also have a heavily polluted day in 19^{th} March 2010 [Li et al., 2012].The aim of this work was to (1) evaluate the ability of the weather research and forecasting model with chemistry (WRF-Chem) to reproduce East Asian dust relative to observational data; (2) investigate the dynamic and thermodynamic mechanisms of dust emission and transport over the TD and GD; (3) elucidate the influence of TD and GD dust throughout East Asia; and (4) estimate the direct radiation forcing induced by the TD and GD dust over East Asia. The paper is organized as follows. The model and observational data are described in Sections 2 and 3. The model evaluation and a discussion of the emission and transport of East Asian dust are presented in Section 4. The radiative forcing of dust is estimated in Section 5 followed by the discussion and conclusions in Section 6.

2. Model description

WRF-Chem, which simultaneously simulates trace gases, particulate materials and meteorological fields [Skamarock et al., 2008], was used in this study. Gas-phase chemical mechanisms, photolysis schemes and aerosols schemes are incorporated into the WRF-Chem model, which considers a variety of coupled physical and chemical processes such as emission, transport (advection, diffusion, and convection), dry/wet deposition, chemical transport, aerosol interactions, and radiation budget [Grell et al., 2005]. Compared with other numerical models, the "online" coupling of meteorology and chemistry in the WRF model more accurately represents the evolution of trace gases and aerosols and permits the inclusion of detailed feedback processes for weather or climate change. Details of the model and relevant references can be found at http://www.pnl.gov/atmospheric/research/wrf-chem/ and http://www.pnl.gov/atmospheric/research/wrf-chem/publications.stm， respectively.

The Regional Acid Deposition Model version 2 chemical mechanism and Model Aerosol Dynamics Model for Europe and Secondary Organic Aerosol Model (MADE/SORGAM) aerosol model [Ackermann et al., 1998; Schell et al., 2001] were implemented by Grell et al. [2005] into WRF-Chem, which includes some aqueous reactions and complex treatments of aerosol radiative properties. MADE/SORGAM model uses the modal approach with Aitken, accumulation, and coarse modes to represent the aerosol size distribution. The aerosol species include mineral dust, sulfate, nitrate, ammonium, black carbon, organic compounds, and sea salt. Aerosol optical properties (e.g., single-scattering albedo, asymmetry factor, and extinction) are computed as a function of wavelength. Furthermore, each chemical constituent of the aerosol is associated with a complex index of refraction [Barnard et al., 2003].

The Goddard Chemistry Aerosol Radiation and Transport (GOCART) dust emission scheme [Ginoux et al., 2001] was coupled with MADE/SORGAM in the WRF-Chem model [Zhao et al., 2010]. Additional details about the GOCART dust emission scheme in the WRF-Chem model can be found in Chen et al. [2013 and 2014]. An emission inventory of anthropogenic, biomass burning, biogenic, and volcanic emissions is also included in the simulation. The anthropogenic emissions of carbon monoxide, nitrogen oxides, SO_2, volatile organic compounds, black carbon, organic carbon, $PM_{2.5}$, and PM_{10} were taken from the 2006 emission inventory developed by David Street (http://www.cgrer.uiowa.edu/EMISSION_DATA_new/index_16.html). The biomass burning emissions were obtained from the Global Fire Emissions Database, Version 3 and have a monthly temporal resolution and 0.5° spatial resolution [van der Werf et al., 2010].

Fig. 1a illustrates the modelling domain which covered the entirety of East Asia (10.8°N~59.6°N, 51.9°E~154.3°E) with a horizontal grid interval of 36 km and 138×187 grid cells. This domain covered dust source regions over East Asia represented by erodibility in WRF-Chem model, as shown in Fig. 1b. The model atmosphere was divided into 35 vertical layers, and the model top pressure was 100 hPa. To reduce the computational time for the simulation, the integration period was 1st-23rd March 2010. Only the results from 18th-23rd March 2010 were used in this study (hereafter referred to as the simulation period). The meteorological initial and boundary conditions were constructed from the National Center for Environmental Prediction final analysis (NCEP/FNL) data at a 6-h temporal interval and 1° horizontal resolution. The NOAA land surface model [Chen et al., 1996; Chen and Dudhia, 2001] and the Yonsei University planetary boundary scheme [Hong, Noh and Dudhia, 2006] were used in the simulation. The Morrison two-moment microphysics scheme [Morrison et al., 2005] and Kain-Fritsch convective scheme [Kain et al., 1990 and Kain et al., 2004] were also used to represent cloud microphysics and convection processes [Zhao et al., 2013] in the simulation. To produce a more realistic simulation of the large-scale circulation situation and main weather systems, the modelled u- and v-wind components and atmospheric temperatures were nudged towards the NCEP/FNL analysis data with a nudging time scale of 6 h [Stauffer and Seaman, 1990].

3. Observations

3.1 CALIPSO Aerosol Extinction Coefficients

The aerosol extinction profiles retrieved by the CALIPSO satellite were used in the study. The CALIPSO satellite, launched in April 2006 to investigate the vertical structure of aerosols and clouds, carries the Cloud-Aerosol Lidar with Orthogonal Polarization (CALIOP) instrument [Winker et al., 2006, 2007]. In this work, the observed aerosol extinction from the CALIPSO level 2 5 km Cloud and Aerosol Profile Products version 3.3 was analyzed. The retrievals were used to evaluate the simulated vertical structure of dust particles along the orbital path at 20:08 UTC on 19th March 2010 in the study. The data for clouds and stratospheric features by the atmospheric volume description and cloud aerosol discrimination score was screened [Liu et al., 2004]. Features with cloud aerosol discrimination scores exceeding 80 were selected for this work, which provided a confidence for the classification of dust layers using the CALIOP cloud-aerosol discrimination algorithm.

3.2 Aerosol Robotic Network (AERONET) AOD

AERONET is a global ground-based aerosol monitoring network established by the National Aeronautics and Space Administration, and

Photometry for Operational Satellite Processing Standards of the National Center for Scientific Research involves standardized automatic sun photometers that measure sun and sky radiances at several wavelengths in the visible and near-infrared bands. The observed radiances are further processed to retrieve aerosol properties via algorithms developed by Dubovik and King (2000) and Dubovik et al. (2002). Global aerosol optical depth is provided in near real time after calibration, processing and distribution. AOD data products are available at three levels based on data quality: unscreened data (Level 1.0), cloud-screened data (Level 1.5), and quality-assured and cloud screened data (Level 2.0). In this work, the level 2.0 products of AOD at SACOL, Mt. Waliguan (Mt_WLG), Taihu, Gwangju_GIST, Shirhuma and Ussuriysksites (Fig. 1a and Table 1) were used to evaluate the simulated AODs over the dust source regions and remote regions.

4. Results and discussions

4.1 Meteorological conditions

To evaluate the model performance in simulating dust emission and transport during the dust storm event, we first compared the simulated meteorological conditions against the reanalysis data and in situ measurements. The average wind and temperature fields at 500 hPa from the NCEP/FNL reanalysis data and WRF-Chem simulations over East Asia during the simulation period are shown in Fig. 2. Generally, WRF-Chem model reproduced the large-scale circulation field over East Asia extremely well, including the location and shape of the East Asian subtropical westerly jet stream, the lower-latitude edges of the westerly jet, and the upper-level westerly jet over East Asia (Fig. 2a). As to the wind speed, the WRF-Chem model was able to simulated it well over TD, GD and eastern and southern China, where the differences with observation were only -0.6~0.6 m s^{-1}. The wind speed over the surrounding area of TD and TP was overestimated with the value of 1.2~3 m s^{-1} due to the complex terrain (Fig. 2b). The differences of temperature at 500 hPa between WRF-Chem model and NCEP/FNL reanalysis data over East Asia were also demonstrated in Fig. 2d. In general, the simulated temperature was almost consistent with the reanalysis data, especially in the eastern, southern and northwestern China. There were slightly underestimated values (-0.4~-0.6 ℃) over GD and extended to the surrounding areas of TD. Moreover, the WRF-Chem model can't simulate air temperature at 500 hPa over the TP well. The bias was up to -1.3℃ in the north slope of the TP that is beyond the scope of this study.

Wind rose diagrams for four meteorological stations including Tazhong over the TD and Guaizihu, Yumenzhen, and Mazongshan over the GD (Fig. 1a and Table 1) are shown in Fig. 3. The hourly 10-m wind observations were obtained from the Chinese National Meteorological Center and will be referred to as observed wind direction and wind speed records. The winds mainly blowed from west to east at the Tazhong site during the dust event. The wind speeds generally exceeded 2 m s^{-1}. The frequency of calm winds accounted for 8.0% of total wind records. The average magnitude of the observed wind speed at the Tazhong site (3.4 m s^{-1}) was lower than the average value of the simulations (5.2 m s^{-1}). Over the GD, the wind speeds were primarily between 3-10 m s^{-1}. The average wind speed exceeded that at the Tazhong site. At the Guaizihu site，the prevailing wind direction was from the west and the northwest. The simulated wind speed was slightly higher than the observed wind speed. At the Yumenzhen site，the prevailing wind direction was generally from the east. The simulated wind speed (6.4 m s^{-1}) was higher than the observed wind speed (4.7 m s^{-1}). The Mazongshan site is west of the Guaizihu site. At this site the simulations did not capture the easterly component of the winds well.

Generally, WRF-Chem simulations reproduced the wind field at the surface in the dust source regions. However, the simulated wind speed at 10 m (4.2 m s^{-1} over the TD and 6.4 m s^{-1} over the GD) was slightly higher than the observed wind speed (3.5 m s^{-1} over the TD and 5.7 m s^{-1}). In addition, the frequency of calm winds in Tazhong and Guaizihu was 8.0% and 0.5%, respectively. The simulation results did not describe the calm winds well in these regions. It should be noted that the different frequencies of wind speed and direction between the observational records and numerical model might have contributed to the deviations in the results. Chen et al. (2014a) have analyzed the monthly averages of the 10-m winds over the TD and GD from observations, reanalysis data, and WRF-Chem simulations during 2007-2011. They also found that the WRF-Chem model could reproduce the observed seasonal and inter-annual variations of wind field over the TD and GD. However, the simulations misestimated the observed wind speed because of WRF model limitations in representing sub-grid variations and turbulence processes in the complex terrain and land surface types [Hanna et al., 2000]. This is a common issue in WRF simulations, which will be improved in a newer version of the WRF model through the use of surface drag parameterization [Chen et al., 2014; Jiménez and Dudhia, 2012]. Although simulations overestimate the magnitude of observed 10-m wind speed over the TD and GD, it could reproduce the observed spatial distribution of 10-m wind speed in dust source regions. Therefore, we could tune the value of the empirical proportionality constant C in the GOCART dust emission schemes to keep the magnitude of modeled AOD consistent with the observational data.

4.2 Spatial and temporal distribution of dust

The modelled dust optical properties were compared with those from surface observation reports and satellite retrievals to validate WRF-Chem model results. Fig. 4 shows spatial distributions of daily mean 550 nm AOD from MODIS and the corresponding WRF-Chem simulations over East Asia. The time series of the observed and modelled AODs at the six AERONET sites (SACOL, Taihu, Mt_WLG, Ussuriysk, Gwangju_GIST, and Shirahama in Fig. 1a and Table 2) are shown in Fig. 5. In addition, the vertical profile of dust aerosols is the critical factor that determines radiative forcing and climate response from mineral dust [Huang et al., 2008]. The accurate estimates of the vertical structure make sense to reveal the variation of the dust optical properties and dust long-term transport mechanism. Cross-sections of aerosol extinction coefficients at 532 nm over the TD at 20:08 UTC (2:08 LT) on 19th March 2010 from the WRF-Chem model and CALIPSO retrievals is shown in Fig. 6.

Generally, MODIS retrievals could be compared to the simulated AOD over East Asia, although datasets were not insufficient because of their limited spatial and temporal coverage. The modelling results generally captured the observed AODs from the MODIS retrievals over the dust source region, indicating that the GOCART dust emissions represented the dust source function over East Asia well. The average MODIS AOD and simulated AODs over the TD and GD were 0.88 and 0.82, respectively. However, the simulated AOD was lower than the MODIS AOD in the southwestern part of the domain, probably because of the anthropogenic emissions in northern India were underestimated in the simulation (Fig. 4).

The peak value center of the dust aerosol occurred in the TD and GD and declined toward the north on 18th March (Fig. 4). The daily average of the observed AOD at SACOL was 0.28, and the corresponding simulated AOD was less than 0.1. Over dust remote regions, the dust AOD accounted for less than 10% of the total AOD. Then, a large amount of dust aerosol was injected, especially over the GD on 19th March. The simulated AODs showed good consistency with those from the ground-based data (Fig. 4). The dust AOD accounted for more than 95% of total AOD at SACOL. The observed AOD was 0.58, which was comparable to the corresponding simulated AOD (0.53) at SACOL.

The observed AOD over the TD exceeded that over the GD by 0.3 on 20th March. The simulated AODs over the GD underestimated the MODIS AODs by up to 0.2 (Fig. 4). The observed AODs at SACOL were higher than the simulated AOD by up to 15% because of the effects of the local emission source. The AODs at SACOL and Mt_Waliguan AOD showed a decreasing trend. However, the dust AODs began to increase at the Taihu, Ussuriysk, and Gwangju_GIST sites, thus indicating that the dust particles from the dust source regions were transported to Japan, Korea, and Russia. The Mt_Waliguan AOD increased rapidly up to 0.5, and the higher dust AOD (0.6±0.14) persisted at the Taihu site on 21st March. On 22nd-23rd March, the TD and GD dust mass loadings greatly weakened. The dust AODs were close to 0, except for the SACOL and Mt_Waliguan sites, which are near the dust source regions (Fig. 45).

Moreover, WRF-Chem model captured the vertical structure of aerosols over and near the TD well (Fig. 6). As is well known, the vertical structure of mineral dust plays an important role in the atmospheric heating rate [Minnis and Cox, 1978; Carlson and Benjamin, 1980], long-wave radiative forcing in clear sky, and short-wave radiative forcing in cloudy sky [Liao and Seinfeld, 1998; Meloni et al., 2005], thereby directly affecting climate systems through changes in cloud height, cloud life and precipitation because of the changes in the radiative balance. Therefore, accurate estimates of the vertical structure can reasonably be used to reveal variations in dust optical properties and long-term dust transport mechanisms.

4.3 Dust emission and transport

The detailed dynamic processes of the strong dust storm event along with the synoptic situation are discussed in the section. The simulation domain was relatively small (Fig. 1a) and the characteristics of the larger scale changes in the atmospheric circulation are not reflected in this discussion. The spatial distributions of the geopotential heights, temperatures and wind circulation at 500 hPa and 850 hPa from the NCEP/FNL reanalysis data are shown in Figs. 7 and 8.

The dust storm was initialized by a cold air intrusion in the northern part of Xinjiang on 18th March. The dense isotherm gradient led to the stronger cold advection. A mass of cold air accumulated in the northern part of the Tianshan Mountains, which decreased the surface temperatures in northern China. The northwest flow along the Tianshan Mountain was then injected into the TD deserts (Figs. 7 and 8). The convergence of the warm and cold air led to the low level convergence, which created dynamic conditions for the TD dust emission. The GD was located in the warmer zone in advance of the cold front, which generated uplift movement and further injected dust particles over the GD (Figs. 7 and 8). The dust layer over the GD accumulated at 850 hPa. The maximum of $PM_{2.5}$ dust concentration reached 41 $\mu g\ m^{-3}$ (Fig. 10). The daily average of the dust emission fluxes over the TD and GD were 20 and 28 μg m^{-2} s^{-1}, respectively (Fig. 9). This result was also consistent with Zhao et al. (2005) and Zhang et al. (2009). Zhao et al. (2005) pointed out that the dust emission over East Asia was about 18 μg m^{-2} s^{-1} in April and 15 μg m^{-2} s^{-1} in May using Northern Aerosol Regional Climate Model. Zhang et al. (2009) calculated the dust emission from 1997 to 2006 and the dust emission of TD along with the surround region was around 23 μg m^{-2} s^{-1} based on the Regional Climate Model RegCM version 3.

Dust emission over GD and TD had reached a maximum on 19th March for the dust event. The stronger cold advection greatly enhanced the atmospheric baroclinicity because the isotherm was almost perpendicular to the isoheight behind the trough. This context aided in the downward transport of momentum produced by the northwest flow in the high levels, which caused the strong wind and dust emissions (Figs. 7 and 8). The $PM_{2.5}$ dust concentrations over the TD reached up to 65 μg m^{-3} (Fig. 10). The GD dust particles were then transported long distances to eastern and southern China because of the high-level northwest flow. Thus, the PM2.5 dust concentrations in downwind regions including Korean Peninsula and Japan increased from 5 to 14 μg m^{-3} at 850 hPa. Cold air climbing over the Tianshan Mountain and joining with the strong northeast cold air over the TD caused a strong northwest wind, which enhanced dust emission over the TD. However, the height of dust layer over the TD (about 2 km) was lower than over the GD (about 4 km) (Fig. 10).

The cold advection behind the trough helped the cold vortex to spread slowly eastwards when the angle between the isotherm and the isoheight was sufficient on 20th March (Fig. 7). Cold air accumulated to the north of the Tianshan Mountains and then climbed over the mountains, spreading northwestwards (Fig. 8). The dust emission over the TD (18.4 μg m^{-2} s^{-1}) was further enhanced by the influence of the anticyclone behind the cold front. As the upper troughs weakened and moved out, the GD dust emission (8.2 μg m^{-2} s^{-1}) began to decrease (Fig. 9). The $PM_{2.5}$ dust concentration decreased to 22±8.2 μg m^{-3} (Fig. 10), thus indicating that the first stage of the dust storm event was essentially complete. The $PM_{2.5}$ dust concentration in eastern China and Korean Peninsula still increased and the maximum value was 26 μg m^{-3}. Dust particles in these downwind regions could reduce visibility, change radiative budget, and further modify atmospheric stability at regional scale [Chen et al. 2014; Kang, et al, 2013].

The period of 21st-23rd March is regarded as the second stage of the dust event. The TD dust emission peaked in this dust storm event on 21st March. The average TD dust emission flux was 37.2±6.4 μg m^{-2} s^{-1} (Fig. 9). The frontal zone in the upper atmosphere gradually moved south to north of 40°N (Fig. 7). Cold air climbed over the Pamir Plateau and intruded into the Tarim basin, which caused strong uplift motion over the TD. The TD dust particles accompanied by the jet stream and cold advection were transported to the most of northern China. However, the strength of the dust emission in this stage was weaker than that on 19th March. The strengthening of the frontal zones gradually decreased and the descending motions typically occurred over a larger area on 22nd-23rd March (Fig. 8). The dust emission flux decreased to 10 μg m^{-2} s^{-1} in the two dust source regions (Fig. 9). Moreover, the prevailing wind is the key factor for producing significant differences in dust emission and long-term transport over the TD and GD (Fig. 11). The TD is located in the basin surrounded on three sides by mountains. And the wind at the low level over the TD is the East wind based. Therefore, TD dust is not easily transported out of the basin, although the TD has the largest dust emission in the second stage of the dust storm event. Compared to the TD, the GD is relatively flat areas. And the strong westerly wind over the GD is advantageous for ejecting and further transporting of GD dust. Sun et al. (2001) have also noted that GD dust can be entrained to an elevation of only <3 km in most cases (about 90%). The relatively lower-elevation dust layers are deposited mainly in inland China.

From the thermodynamic perspective, the GD dust was also more favorable than the TD dust in terms of the dust emission and vertical transport (Fig. 12). Specifically, the temperature profile over the GD from the surface to the 700 hPa was almost parallel to the dry adiabatic rate, indicating that the layer was in an absolutely unstable state, favoring of emission and vertical transport of the GD dust particles. In contrast, the sounding data in the TD revealed an unstable layer quite near the surface that ranged from the surface to a few hundred meters, helping to vertically elevate the TD dust. Nonetheless, the temperature lapse rate decreases with increasing altitude and is less than that in the wet adiabatic rate, indicating the existence an absolutely stable layer and thus requiring more energy to lift an air parcel. Therefore, the vertical movement of the air was inhibited, and the elevation of the dust layer ceased. In addition, the relative humidity in the GD was low within the entire layer, whereas it remained low in the TD in the lower-middle troposphere but increased with height, resulting in a humidity condition that was dryer below and wetter above. This is the hallmark of a conditional stable state, which inhibits the convective movement of the atmosphere.

4.4 Dust budget analysis

To better understand the relative contribution of dust emissions over the TD and GD during the dust storm event, Fig. 13 shows that the budgets for dust emission, transport, and dry and wet depositions over the TD and GD, respectively. The positive sign represents increase to dust concentration and the negative sign represents decrease to dust concentration. Among the four budget terms, the source term of the dust concentration was the absolute dust emission for the entire dust storm event over the TD and GD. Emission contribution is absolute positive. While dry/wet depositions as well as transport are sinks of dust in the atmosphere, these values are always negative. Dry deposition is the largest sink of dust, following by transport and wet deposition.

Specifically, the GD dust emission was the largest contributor to dust concentration over East Asia in the first stage (18^{th}-20^{th} March) (Fig. 13). The daily dust emission flux over the GD peaked above 68 μg m^{-2} s^{-1} (Fig. 9). The contribution of the transport of the GD dust particles (up to 3.4 ton day^{-1}) was much greater than that of the TD dust (up to 1.5 ton day^{-1}) (Fig. 13). Therefore, more GD dust particles could have been transported over East Asia. The strengthening dust emissions weakened substantially in the second stage (21^{st}-23^{rd} March). The TD dust emission exerted an important effect on dust concentrations in that stage. The average TD dust emission flux was 20 ± 4.6 μg m^{-2} s^{-1} (Fig. 9). However, the transport capability of the GD dust was still stronger than that of the TD dust in this stage. In Fig. 14, we can find that the GD dust particles were accumulated under 3 km between 286 K-296 K. The GD dust concentration reached up to 1500 μg m^{-3} (Fig. 14). The mass concentrations of the TD dust in the lower-middle troposphere were lower than that of the GD dust.

4.5 Direct Radiative forcing induced by dust over East Asia

Dust significantly affected radiation budget over East Asia during the dust storm event. The simulation with and without dust particles was used to estimate the magnitude of dust radiative forcing in the study. The shortwave (SW), longwave (LW) and net (SW+LW) direct radiative forcing of dust aerosols at all-sky conditions are calculated at the top of the atmosphere (TOA), surface (SUR) and in the atmosphere (ATM) during the simulation period in Fig. 15. The spatial distribution of dust radiative forcing was similar to that of dust mass loading over East Asia with highest values over the TD and GD. The SW forcing induced by dust at the TOA over East Asia was generally negative with greatest values of -6 to -8 W m^{-2} and -2 to -4 W m^{-2} over the GD and TD, respectively. Compared with dust aerosol over the Sahara desert, East Asian dust has a complex refractive index with small imaginary part and the back scattering of dust particles is relatively strong, which lead to the high negative values of SW radiation forcing at the TOA [Wang et al., 2004; Jin et al., 2015]. The magnitude of direct radiative forcing at the TOA was dominated by the SW radiative forcing because the LW radiative forcing induced by dust was much smaller (0~1 W m^{-2}). The maximum net radiative forcing value at the TOA reached -10 W m^{-2} in southern Inner Mongolia, larger than over the TD (-5 W m^{-2}), which was consistent with the conclusion of Chen et al. (2014) with the values of -8.3 W m^{-2} and -5.2 W m^{-2} over the GD and TD, respectively.

The SW cooling effect of the dust was predominant at the surface exceeding -8 W m^{-2} in northern China, which was much stronger than the LW warming effect (+2 to +8 W m^{-2}). The region of significant LW radiative forcing occurred mainly over the TD and GD while the SW radiative forcing almost covered the whole northern China with a higher value. As a result, the dust caused a strong cooling effect at the surface since dust aerosols weakened the incoming radiation through absorption and scattering of dust particles [Kumar et al., 2014; Jin et al., 2015]. The maximum net radiative forcing at the surface was as great as -14 W m^{-2} over the GD and -9.2 W m^{-2} along the dust transport pathway from northern China to Japan and Korean Peninsula, which is similar to the conclusions of Zhang et al (2009). In the atmosphere, the dust aerosol induced positive SW radiative forcing (+1 to +11 W m^{-2}) and negative LW radiative forcing (-1 to -9 W m^{-2}), which led to warming in the atmosphere because of dust absorption. The LW radiative forcing was negative in TD and GD since the dust layers sent LW to TOA. The slightly positive net forcing varied from +4 to +8 W m^{-2} over the TD, +3 to +6 W m^{-2} over the GD, and 0 to +4 Wm^{-2} over eastern China, which showed the warming effect of dust layers in the atmosphere. The average net dust radiative forcing in the atmosphere varied from +1 to +6 W m^{-2} over the downwind regions, including eastern China, Korea and Japan. Therefore, the radiative heating rate of dust has a significant influence on the vertical distribution of temperature of atmosphere. Fig. 16 further illustrated that the vertical profiles of the radiative heating rate induced by dust particles over East Asia. In general, dust induced warming in the atmosphere, especially over the TD and GD. The radiative heating rate was maximum over the GD at 0.14±0.03 K day^{-1} in the 1~3 km layers, where the dust mass loading was greatest, and gradually decreased with height. In comparison, the radiative heating rate peaked in the 1~2 km layers over the TD, exhibiting values ranging from 0.04 to 0.12 K day^{-1}, lower than those of the GD.

5. Summary

The WRF-Chem model was used to investigate a typical dust storm event that occurred from 18th to 23rd March 2010 in the study. WRF-

Chem model is capable of simulating East Asian dust during the simulation period. The spatial and temporal variations of large-scale circulation field and dust aerosols over East Asia were captured by the model. The evaluations provided confidence for further understanding the emission and transport of the TD and GD dust over East Asia based on the simulated results. The results showed that the weather conditions, topographies and surface type of GD and TD are quite different, which may lead to the difference of the dust emission, uplifted height, horizontal and vertical dust flux and long distance transport. The GD dust contributed significantly to the dust concentration over East Asia, especially on 19th March. The GD was located in the warm zone in advance of a cold front. Rapidly warming surface temperatures and cold air advection at high levels caused strong instability in the atmosphere which strengthened the downward momentum transported from the middle and low troposphere and caused strong surface winds and gusts. The ascending motion and strong surface winds provided the energy needed for dust resuspension, lifting and transport over the GD. Moreover, the GD is located at the relatively flat and high altitude regions under the influence of and confluence of the northern and southern westerly winds. Therefore, the GD dust particles were easily lofted to 4 km and transported eastward over Japan and Korean Peninsula. The contribution of transport of the GD dust particles (up to 3.7 ton day^{-1}) was much greater than of the TD dust (up to 0.8 ton day^{-1}) over East Asia in the simulation period.

The TD dust was not easily transported out of the basin because of the complex terrain and the prevailing wind, even if the TD has the larger dust emission. Specifically, the TD is surrounded by mountain ranges that exceed 3 km in height, except for the Hexi corridor opening to the northeast. The process that generated the dust storms was strongly affected by these topographical characteristics in addition to the surface conditions. In addition, the easterly wind dominated the TD areas. Thus, the contribution of the transported TD dust to the dust sink was still smaller than that of the GD dust. However, a small amount of finer dust particles over the TD ($PM_{2.5}$ dust concentration was approximately 8.7 ug m^{-3}) was lifted to 4 km or higher, which were transported long distances from the source regions. The effects of the TD dust were not only local but worked on regions far from the sources as well.

East Asian dust during the dust storm event plays a role in the radiation budget. Generally, compared with previous modeling estimates of direct radiative forcing by dust over East Asia, our estimates are comparable with these modeling studies [Zhang et al., 2009; Han et al., 2012; Chen et al., 2014; Conant et al., 2003; Park et al.,2005]. The net dust radiative forcing over the East Asia was about -6.5 W m^{-2}(-8.4 W m^{-2}) at the TOA (surface) in this study, which is similar to the estimates given by Conant et al. (2003) and Park et al. (2005), about -5 and -8 W m^{-2}(-6 and -11 W m^{-2}) at the TOA (surface), respectively. However, the uncertainties in direct radiative forcing over East Asia are still existed. The biases in estimates of direct radiative forcing in simulations could be attributed to following reasons. First of all, biases from dust emission scheme, dust transport and deposition scheme could greatly affect the assessments of dust radiative forcing in the model. Moreover, differences in the vertical distribution of dust layer, dust particle size distribution, and absorptive characteristics and meteorological conditions could influence on the large differences in the quantitative assessment of dust radiative forcing [Tegen et al., 1996; H Wang et al., 2004, 2007; Wu et al., 2004].

Overall, compared with the TD dust, the importance of the GD dust to dust concentration in eastern China, Japan and Korea is most often neglected. Our study focused primarily on the dynamics and thermodynamics of dust emission and transport over TD and GD and further elucidated the influence of TD and GD dust on the entire East Asia based on a case study using the WRF-Chem model. However, it is necessary to further investigate the quantitative contributions of TD and GD dust for the dust mass concentrations over East Asia for a longer time scale based on sensitivity tests in numerical model. In addition, the climate effects of the GD dust over East Asia are needed to investigate in the future.

Acknowledgments

We acknowledge Chun Zhao and Yun Qian for their help for this work. This research was supported by the Foundation for Innovative Research Groups of the National Science Foundation of China (Grant No. 41521004) and National Natural Science Foundation of China (No. 41405003).

References:

Ackermann, I. J., Hass, H., Memmesheimer, M., Ebel, A., Binkowski, F. S., and Shankar, U.: Modal aerosol dynamics model for Europe, Atmos. Environ., 32, 2981–2999, doi:10.1016/S1352-2310(98)00006-5, 1998.

Barnard, J. C., Fast, J. D., Paredes-Miranda, G., Arnott, W. P., and Laskin, A.: Technical Note: Evaluation of the WRF-Chem “Aerosol Chemical to Aerosol Optical Properties” Module using data from the MILAGRO campaign, Atmos. Chem. Phys., 10, 7325–7340, doi:10.5194/acp-10-7325-2010, 2010.

Bi, J., Huang, J., Fu, Q., Wang, X., Shi, J., Zhang, W., Huang, Z., Zhang, B.: Toward characterization of the aerosol optical properties over Loess Plateau of Northwestern China. Journal of Quantitative Spectroscopy & Radiative Transfer, 112(2):346-360, doi: 10.1016/j.jqsrt.2010.09.006, 2011.

Carlson, T. N. and Benjamin, S. G.: Radiative Heating Rates for Saharan Dust, J. Atmos. Sci., 37, 193–213, doi:10.1175/1520-0469(1980)037<0193:RHRFSD>2.0.CO;2, 1980.

Chen, F. and Dudhia, J.: Coupling an Advanced Land Surface–Hydrology Model with the

Penn State–NCAR MM5 Modeling System. Part I: Model Implementation and Sensitivity, Mon. Weather Rev., 129, 569–585, doi:10.1175/1520-0493(2001)129<0569:CAALSH>2.0.CO;2, 2001.

Chen, F., Mitchell, K., Schaake, J., Xue, Y., Pan, H. L., Koren, V., Duan, Q. Y., Ek, M., and Betts, A.: Modeling of land surface evaporation by four schemes and comparison with FIFE observations, J. Geophys. Res. Atmos., 101(D3), 7251–7268, doi: 10.1029/95JD02165, 1996.

Chen, S., Zhao, C., Qian, Y., Leung, Ruby, L., Huang, J., Huang, Z, W., Bi, J, R., Zhang, W., Shi, J., Yang, L., Li, D., Li, J. : Regional modeling of dust mass balance and radiative forcing over East Asia using WRF-Chem, Aeolian Research.,15,15-30, doi:10.1016/j.aeolia.2014.02.001, 2014.

Chen, S., Huang, J., Zhao, C., Qian, Y., Leung, L. R., and Yang, B.: Modeling the transport and radiative forcing of Taklimakan dust over the Tibetan Plateau: A case study in the summer of 2006, J. Geophys. Res. Atmos., 118, 797–812, doi:10.1002/jgrd.50122, 2013.

Chen, S., Zhao, C., Qian, Y., Leung, L. R., Huang, J., Huang, Z., Bi, J., Zhang, W., Shi, J., Yang, L., Li, D., and Li, J.: Regional modeling of dust mass balance and radiative forcing over East Asia using WRF-Chem, Aeolian Res., 15, 15–30, doi:10.1016/j.aeolia.2014.02.001, 2014.

Chen, S., Huang, J., Qian, Y., Ge, J., and Su, J.: Effects of aerosols on autumn precipitation over Mid-Eastern China, J. Trop. Meteorol., 20, 242–250, 2014.

Dubovik, O. and King, M. D.: A flexible inversion algorithm for retrieval of aerosol optical properties from Sun and sky radiance measurements, J. Geophys. Res. Atmos., 105(D16), 20673–20696, doi: 10.1029/2000JD900282, 2000.

Dubovik, O., Holben, B., Eck, T. F., Smirnov, A., Kaufman, Y. J., King, M. D., Tanré, D., and Slutsker, I.: Variability of Absorption and Optical Properties of Key Aerosol Types Observed in Worldwide Locations, J. Atmos. Sci., 59, 590–608, doi:10.1175/1520-0469(2002)059<0590:VOAAOP>2.0.CO;2, 2002.

Eguchi, K., Uno, I., Yumimoto, K., Takemura, T., Shimizu, A., Sugimoto, N., and Liu, Z.: Trans-pacific dust transport: integrated analysis of NASA/CALIPSO and a global aerosol transport model, Atmos. Chem. Phys., 9, 3137–3145, doi:10.5194/acp-9-3137-2009, 2009.

Fu, Q., Thorsen, T J., Su, J., Ge, J., Huang, J.: Test of Mie-based single-scattering properties of non-spherical dust aerosols in radiative flux calculations. Journal of Quantitative Spectroscopy & Radiative Transfer, 110(14–16):1640-1653, doi: 10.1016/j.jqsrt.2009.03.010, 2009

Ginoux, P., Chin, M., Tegen, I., Prospero, J. M., Holben, B., Dubovik, O., and Lin, S. J.: Sources and distributions of dust aerosols simulated with the GOCART model, J.

Geophys. Res., 106(D17), 20255, doi: 10.1029/2000JD000053, 2001.

Grell, G. A., Peckham, S. E., Schmitz, R., McKeen, S. A., Frost, G., Skamarock, W. C., and Eder, B.: Fully coupled “online” chemistry within the WRF model, Atmos. Environ., 39, 6957–6975, doi:10.1016/j.atmosenv.2005.04.027, 2005..

Ge, J., J., Huang, C., Xu, Y., Qi, and H., Liu: Characteristics of Taklimakan dust emission and distribution: A satellite and reanalysis field perspective. Journal of Geophysical Research: Atmospheres, 119, 11,772–11,783, doi:10.1002/2014JD022280, 2014.

Han, Z., Li, J., Xia, X., Zhang, R.: Investigation of direct radiative effects of aerosols in dust storm season over East Asia with an online coupled regional climate-chemistry-aerosol model, Atmos. Environ.,54,688-699, doi:10.1016/j.atmosenv.2012.01.041,2012.

Hanna, S. R., Yang, R., and Yin, X.: Evaluations of numerical weather prediction (NWP) models from the point of view of inputs required by atmospheric dispersion models, Int. J. Environ. Pollut., 14, 98–105, doi:10.1504/IJEP.2000.000530, 2000.

Hong, S. Y., Noh, Y., and Dudhia, J.: A New Vertical Diffusion Package with an Explicit Treatment of Entrainment Processes, Mon. Weather Rev., 134, 2318–2341, doi:10.1175/MWR3199.1, 2006.

Hsu, N. C., Tsay, S. C., King, M. D., and Herman, J. R.: Deep Blue Retrievals of Asian Aerosol Properties during ACE-Asia, IEEE Trans. Geosci. Remote Sens., 44, 3180–3195, doi:10.1109/TGRS.2006.879540, 2006.

Huang, J., Lin, B., Minnis, P., Wang, T., Wang, X., Hu, Y., Yi, Y., and Ayers, J. K.: Satellite-based assessment of possible dust aerosols semi-direct effect on cloud water path over East Asia, Geophys. Res. Lett., 33, L19802, doi:10.1029/2006GL026561, 2006a.

Huang, J., Wang, Y., Wang, T., and Yi, Y.: Dusty cloud radiative forcing derived from satellite data for middle latitude regions of East Asia, Prog. Nat. Sci., 16, 1084–1089, doi:10.1080/10020070612330114,2006b.

Huang, J., Minnis, P., Lin, B., Wang, T., Yi, Y., Hu, Y., Sun-Mack, S., and Ayers, K.: Possible influences of Asian dust aerosols on cloud properties and radiative forcing observed from MODIS and CERES, Geophys. Res. Lett., 33, L06824, doi:10.1029/2005GL024724, 2006c.

Huang, J., Minnis, P., Yi, Y., Tang, Q., Wang, X., Hu, Y., Liu, Z., Ayers, K., Trepte, C., and Winker, D.: Summer dust aerosols detected from CALIPSO over the Tibetan Plateau, Geophys. Res. Lett., 34, L18805, doi:10.1029/2007GL029938, 2007.

Huang, J. P., Huang, Z. W., Bi, J. R., Zhang, W., and Zhang, L.: Micro-pulse lidar measurements of aerosol vertical structure over the Loess Plateau, Atmos. Ocean. Sci. Lett., 1, 8–11, doi:10.1080/16742834.2008.11446756, 2008a.

Huang, J., Minnis, P., Chen, B., Huang, Z., Liu, Z., Zhao, Q., Yi, Y., and Ayers, J. K.: Long-range transport and vertical structure of Asian dust from CALIPSO and surface measurements during PACDEX, J. Geophys. Res., 113(D23), D23212, doi:10.1029/2008JD010620, 2008b.

Huang, J., Zhang, W., Zuo, J., Bi, J., Shi, J., Wang, X., Chang, Z., Huang, Z., Yang, S., Zhang, B., Wang, G., Feng, G., Yuan, J., Zhang, L., Zuo, H., Wang, S., Fu, C., and Jifan, C.: An overview of the Semi-arid Climate and Environment Research Observatory over the Loess Plateau, Adv. Atmos. Sci., 25, 906–921, doi:10.1007/s00376-008-0906-7, 2008c.

Huang, J., Fu, Q., Su, J., Tang, Q., Minnis, P., Hu, Y., Yi, Y., and Zhao, Q.: Taklimakan dust aerosol radiative heating derived from CALIPSO observations using the Fu-Liou radiation model with CERES constraints, Atmos. Chem. Phys., 9, 4011–4021, doi:10.5194/acp-9-4011-2009, 2009.

Huang, J., Minnis, P., Yan, H., Yi, Y., Chen, B., Zhang, L., and Ayers, J. K.: Dust aerosol effect on semi-arid climate over Northwest China detected from A-Train satellite measurements, Atmos. Chem. Phys., 10, 6863–6872, doi:10.5194/acp-10-6863-2010, 2010.

Huang, J., Fu, Q., Zhang, W., Wang, X., Zhang, R., Ye, H., and Warren, S. G.: Dust and Black Carbon in Seasonal Snow Across Northern China, Bull. Am. Meteorol. Soc., 92, 175–181, doi:10.1175/2010BAMS3064.1, 2011.

Huang, J., Guan, X., and Ji, F.: Enhanced cold-season warming in semi-arid regions, Atmos. Chem. Phys., 12(, 5391–5398, doi:10.5194/acp-12-5391-2012, 2012.

Huang, J., Wang, T., Wang, W., Li, Z., and Yan, H.: Climate effects of dust aerosols over East Asian arid and semiarid regions, J. Geophys. Res. Atmos., 119, 11,398–11,416, doi:10.1002/2014JD021796, 2014.

Huang, J., Yu, H., Guan, X., Wang, G., and Guo, R.: Accelerated dryland expansion under climate change, Nat. Clim. Chang., 6, 166–171 [online] Available from: doi:10.1038/nclimate2837, 2016.

Huang, X. X., Wang, T. J., Jiang, F., Liao, J. B., Cai, Y. F., Yin, C. Q., Zhu, J. L., and Han, Y.: Studies on a severe dust storm in East Asia and its impact on the air quality of Nanjing, China, Aerosol Air Qual. Res., 13, 179–193, doi:10.4209/aaqr.2012.05.0108, 2013.

Huang, Z., Huang, J., Bi, J., Wang, G, Wang, W, Fu, Q., Li, Z., Tsay, S., Shi, J.: Dust aerosol vertical structure measurements using three MPL lidars during 2008 China-U.S. joint dust field experiment. J. Geophys. Res. Atmos., 115(D7):1307-1314, doi: 10.1029/2009JD013273, 2010.

Jiménez, P. A. and Dudhia, J.: Improving the Representation of Resolved and Unresolved Topographic Effects on Surface Wind in the WRF Model, J. Appl. Meteorol. Climatol., 51, 300–316, doi:10.1175/JAMC-D-11-084.1, 2012.

Jin, Q., Wei, J., Yang, Z.-L., Pu, B., and Huang, J.: Consistent response of Indian summer monsoon to Middle East dust in observations and simulations, Atmos. Chem. Phys., 15, 9897-9915, doi: 10.5194/acp-15-9897-2015, 2015.

Kain, J. S.: The Kain–Fritsch Convective Parameterization: An Update, J. Appl. Meteorol., 43, 170–181, doi:10.1175/1520-0450(2004)043<0170:TKCPAU>2.0.CO;2, 2004.

Kain, J. S. and Fritsch, J. M.: A One-Dimensional Entraining/Detraining Plume Model and Its Application in Convective Parameterization, J. Atmos. Sci., 47, 2784–2802, doi:10.1175/1520-0469(1990)047<2784:AODEPM>2.0.CO;2, 1990.

Kaufman, Y. J., Wald, A. E., Remer, L. A., Gao, B. C., Li, R. R., and Flynn, L.: The MODIS 2.1-mm channel-correlation with visible reflectance for use in remote sensing of aerosol, IEEE Trans. Geosci. Remote Sens., 35, 1286–1298, doi:10.1109/36.628795, 1997.

Koren, I., Kaufman, Y. J., Remer, L. A., and Martins, J. V: Measurement of the effect of Amazon smoke on inhibition of cloud formation., Science, 303, 1342–1345, doi:10.1126/science.1089424, 2004.

Kurosaki, Y., and Mikami, M.: Threshold wind speed for dust emission in East Asia and its seasonal variations, J. Geophys. Res., 112, D17202, doi:10.1029/2006JD007988, 2007.

Li, Z., Li, C., Chen, H., Tsay, S. C., Holben, B., Huang, J., Li, B., Maring, H., Qian, Y., Shi, G., Xia, X., Yin, Y., Zheng, Y., and Zhuang, G.: East Asian Studies of Tropospheric Aerosols and their Impact on Regional Climate (EAST-AIRC): An overview, J. Geophys. Res., 116, D00K34, doi:10.1029/2010JD015257, 2011.

Li, J., Z., Wang, G., Zhuang, G., Luo, Y., Sun, and Q., Wang.: Mixing of Asian mineral dust with anthropogenic pollutants over East Asia: a model case study of a super-dust storm in March 2010. Atmos. Chem. Phys., 12, 7591–7607, doi:10.5194/acp-12-7591-2012, 2012.

Liao, H. and Seinfeld, J. H.: Radiative forcing by mineral dust aerosols: Sensitivity to key variables, J. Geophys. Res. Atmos., 103(D24), 31637–31645, doi:10.1029/1998JD200036, 1998.

Liu, Z., Vaughan, M. A., Winker, D. M., Hostetler, C. A., Poole, L. R., Hlavka, D., Hart, W. and McGill, M.: Use of probability distribution functions for discriminating between clouds and aerosol in lidar backscatter data, J. Geophys. Res. D Atmos., 109(15), doi:10.1029/2004JD004732, 2004.

Meloni, D., di Sarra, A., Di Iorio, T., and Fiocco, G.: Influence of the vertical profile of Saharan dust on the visible direct radiative forcing, J. Quant. Spectrosc. Radiat.Transf., 93, 397–413, doi:10.1016/j.jqsrt.2004.08.035, 2005.

Minnis, P. and Cox, S. K.: Magnitude of the radiative effects of the Sahara dust layer, Atmos. Sci. Pap. 283, 111 pp., Colo. State Univ., Ft. Collins, Colo., 1978.

Morrison, H., Curry, J. A., and Khvorostyanov, V. I.: A New Double-Moment Microphysics Parameterization for Application in Cloud and Climate Models. Part I: Description, J. Atmos. Sci., 62, 1665–1677, doi:10.1175/JAS3446.1, 2005.

Martonchik, J. V., Diner, D. J., Crean, K., and Bull, M.: Regional aerosol retrieval results from MISR, IEEE Trans. Geosci. Remt. Sensing., 40, 1520-1531, 2002.

Martonchik, J. V., Diner, D. J., Kahn, R. A., Gaitley, B. J., and Holben, B. N.: Comparison of MISR and AERONET aerosol optical depths over desert sites, Geophys. Res. Let., 31, L16102, doi:10.1029/2004GL019807, 2004.

Qian, Y., Gong, D., Fan, J., Leung, L. R., Bennartz, R., Chen, D., and Wang, W.: Heavy pollution suppresses light rain in China: Observations and modeling, J. Geophys. Res., 114(D7), D00K02, doi:10.1029/2008JD011575, 2009.

Ramanathan, V., Crutzen, P. J., Kiehl, J. T., and Rosenfeld, D.: Aerosols, climate, and the hydrological cycle., Science, 294, 2119–24, doi:10.1126/science.1064034, 2001.

Rea, D. K.: The paleoclimatic record provided by eolian deposition in the deep sea: The geologic history of wind, Rev. Geophys., 32, 159-195, doi:10.1029/93RG03257, 1994.

Shao, Y., Ishizuka, M., Mikami, M., and Leys, J. F.: Parameterization of size-resolved dust emission and validation with measurements, J. Geophys. Res.,116,D08203,doi: 10.1029/2010JD014527, 2011.

Schell, B., Ackermann, I. J., Hass, H., Binkowski, F. S., and Ebel, A.: Modeling the formation of secondary organic aerosol within a comprehensive air quality model system, J. Geophys. Res. Atmos., 106(D22), 28275–28293, doi:10.1029/2001JD000384, 2001.

Stauffer, D. R. and Seaman, N. L.: Use of Four-Dimensional Data Assimilation in a Limited-Area Mesoscale Model. Part I: Experiments with Synoptic-Scale Data, Mon. Weather Rev., 118, 1250–1277, doi:10.1175/1520-0493(1990)118<1250:UOFDDA>2.0.CO;2, 1990.

Skamarock, W. C., Klemp, J. B., Dudhia, J., Gill, D. O., Baker, D. M., Duda, M. G., Huang, X., Wang, W., and Powers, J. G.: A description of the Advanced Research WRF version 3:Mesoscale and Microscale Meteorology Division, National Center for Atmospheric Research, Boulder, Colorado, USA, 113, 2008.

Su, J., Huang, J., Fu, Q., Minnis, P., Ge, J., and Bi, J.: Estimation of Asian dust aerosol effect on cloud radiation forcing using Fu-Liou radiative model and CERES measurements, Atmos. Chem. Phys., 8, 2763–2771, doi:10.5194/acp-8-2763-2008, 2008.

Sun, J., Zhang, M., and Liu, T.: Spatial and temporal characteristics of dust storms in China and its surrounding regions, 1960-1999: Relations to source area and climate, J. Geophys. Res. Atmos., 106(D10), 10325–10333, doi:10.1029/2000JD900665, 2001.

Takamura, T., T. Nakajima, and SKYNET community group: Overview of SKYNET and its Activities. Opt. Pura y Apl., 37, 3303–3308, 2004

Takamura, T., N. Sugimoto, A. Shimizu, A. Uchiyama, A. Yamazaki, K. Aoki, T. Nakajima, B. J. Sohn, and H. Takenaka.: Aerosol radiative characteristics at Gosan, Korea, during the atmospheric brown cloud East Asian regional experiment 2005. J. Geophys. Res., 112

, D22S36, doi:10.1029/2007JD008506, 2007.

Tsunematsu, N.: Observed dust storm in the Taklimakan Desert on April 13, 2002. Sci. Online Lett. Atmos., 1, 21–24,doi:10.2151/sola.2005-006,2005.

Uno, I., Amano, H., Emori, S., Kinoshita, K.., Matsui, I., and Sugimoto, N.: Trans-Pacific yellow sand transport observed in April 1998: A numerical simulation, J. Geophys. Res. Atmos., 106(D16), 18331–18344, doi:10.1029/2000JD900748, 2001.

van der Werf, G. R., Randerson, J. T., Giglio, L., Collatz, G. J., Mu, M., Kasibhatla, P. S., Morton, D. C., DeFries, R. S., Jin, Y., and van Leeuwen, T. T.: Global fire emissions and the contribution of deforestation, savanna, forest, agricultural, and peat fires (1997–2009), Atmos. Chem. Phys., 10, 11707–11735, doi:10.5194/acp-10-11707-2010, 2010.

Wang, H., Zhang, X. Y., Gong, S. L., Chen, Y., Shi G. Y., and Li, W.: Radiative feedback of dust aerosols on the East Asian dust storms, J. Geophys. Res., 115, D23214, doi:10.1029/2009JD013430, 2010.

Wang, H., Shi, G. Y., Teruo, A., Wang, B., and Zhao, T. L.: Radiative forcing due to dust aerosol over east Asia-north Pacific region during spring 2001, Chin. Sci. Bull., 49, 2212–2219, 2004.

Wang, J., Xu, X., Henze, D K., Zeng, J., Ji, Q., Tsay, S., Huang, J.: Top-down estimate of dust emissions through integration of MODIS and MISR aerosol retrievals with the GEOS-Chem adjoint model. Geophys. Res. Lett., 39(8):142-148, doi: 10.1029/2012GL051136, 2012.

Wang, X., Huang, J., Zhang, R., Chen, B., Bi, J.: Surface measurement of aerosol properties over northwest China during ARM China 2008 deployment. J. Geophys. Res. Atmos., 115(11):2333-2338, doi: 10.1016/j.jqsrt.2010.09.006, 2010.

Winker, D., Pelon, J., and Mc Cormick, M.: Initial results from CALIPSO, 23rd International Laser Radar Conference, Nara, Japan, 2006.

Ye, H., R.Z., Zhang, J.S., Shi, J.P., Huang, S. W., Q. Fu: Black carbon in seasonal snow across northern Xinjiang in northwestern China, Environmental Research Letters, 7(4):044002, 2012.

Winker, D., Hunt, W., and Mc Gill, M.: Initial performance assessment of CALIOP, Geophys.Res. Lett., 34(19), doi:10.1029/2007GL030135, 2007.

Zhang, Y., Takahashi, M., and Guo, L.: Analysis of the East Asian Subtropical Westerly Jet Simulated by CCSR/NIES/FRCGC Coupled Climate System Model, J. Meteorol. Soc. Japan. Ser. II, 86, 257–278, doi:10.2151/jmsj.86.257, 2008.

Zhang, X. Y., Gong, S. L., Zhao, T. L., Arimoto, R., Wang, Y. Q., and Zhou, Z. J.: Sources of Asian dust and role of climate change versus desertification in Asian dust emission, Geophys. Res. Lett., 30, NO.24,2272,doi:10.1029/2003GL018206, 2003.

Zhao, C., Chen, S., Leung, L. R., Qian, Y., Kok, J. F., Zaveri, R. A., and Huang, J.:

Uncertainty in modeling dust mass balance and radiative forcing from size parameterization, Atmos. Chem. Phys., 13, 10733–10753, doi:10.5194/acp-13-10733-2013, 2013.

Zhao, C., Liu, X., and Leung, L. R.: Impact of the Desert dust on the summer monsoon system over Southwestern North America, Atmos. Chem. Phys., 12, 3717–3731, doi:10.5194/acp-12-3717-2012, 2012.

Zhao, C., Liu, X., Leung, L. R., Johnson, B., McFarlane, S. A., Gustafson, W. I., Fast, J. D., and Easter, R.: The spatial distribution of mineral dust and its shortwave radiative forcing over North Africa: modeling sensitivities to dust emissions and aerosol size treatments, Atmos. Chem. Phys., 10, 8821–8838, doi:10.5194/acp-10-8821-2010, 2010.

Zhao, C., Liu, X., Ruby Leung, L., and Hagos, S.: Radiative impact of mineral dust on monsoon precipitation variability over West Africa, Atmos. Chem. Phys., 11, 1879–1893, doi:10.5194/acp-11-1879-2011, 2011.

Zhao, T. L., Gong, S. L., Zhang, X. Y., Blanchet, J. P., McKendry,I. G., and Zhou, Z. J.:A simulated climatology of Asian dust aerosol and its trans-Pacific transport. Part I: Mean climate and validation, J. Climate, 19, 88–103, 2006.

Zhao, T. L., Gong, S. L., Zhang, X. Y., and Mckendry, I.G.:Modeled size-segregated wet and dry deposition budgets of soil dust aerosol during ACE-Asia 2001: Implications for trans-Pacific transport, J. Geophys. Res., 108, 8665, doi:10.1029/2002JD003363, 2003.

Zhang, X.Y., Gong, S.L., Zhao, T.L., Arimoto, R., Wang, Y.Q., Zhou, Z.J.:Sources of Asian dust and role of climate change versus desertification in Asian dust emission. Geophys. Res. Lett. 30 (24), 2272, doi:10.1029/ 2003GL018206, 2003.

Table1 Information about the 10-m wind stations from the Chinese National Meteorological Center (CNMC)

Name	Latitude (°N)	Longitude (°E)	Elevation (m)
Tazhong	39.00	83.40	1099.3
Guaizihu	41.22	102.22	960.0
Yumenzhen	40.16	97.02	1527.0
Maoyinbadao	40.10	104.18	1325.9

Table 2 Information about selected AERONET stations

Name	Latitude (°N)	Longitude (°E)	Elevation (m)
SACOL (China)	35.95	104.14	1965.8
Mt_Waliguan (China)	36.28	100.90	3816.0
Taihu (China)	31.42	120.22	20.0
Gwangju_GIST(Korea)	35.23	126.84	52.0
Shirhuma (Japan)	33.69	135.36	10.0
Ussuriysk(Russia)	43.70	132.16	280.0

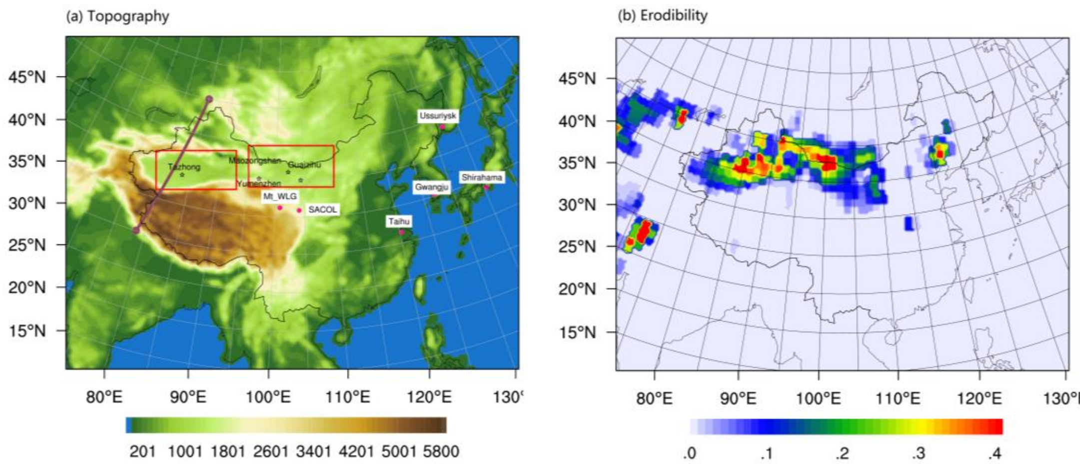

Fig. 1 (a) Modelling domain and spatial distribution of the topography over East Asia. Taklimakan Desert (TD) and Gobi Desert (GD) are indicated by the red boxes. The pink dots are the AERONET sites (SACOL, Mt. Waliguan (Mt_WLG), Taihu, Gwangju_GIST, Shirhuma and Ussuriysk). The black stars are the sites with observed 10-m winds (Tazhong, Maozongshan, Yumenzhen, and Guaizihu). The blown line represents the orbit path of CALIPSO/CALIOP over the TD at 0:08 UTC (2:08 LT) on 19th March 2010. (b) Soil erodibility used in GOCART dust emission scheme from WRF-Chem model.

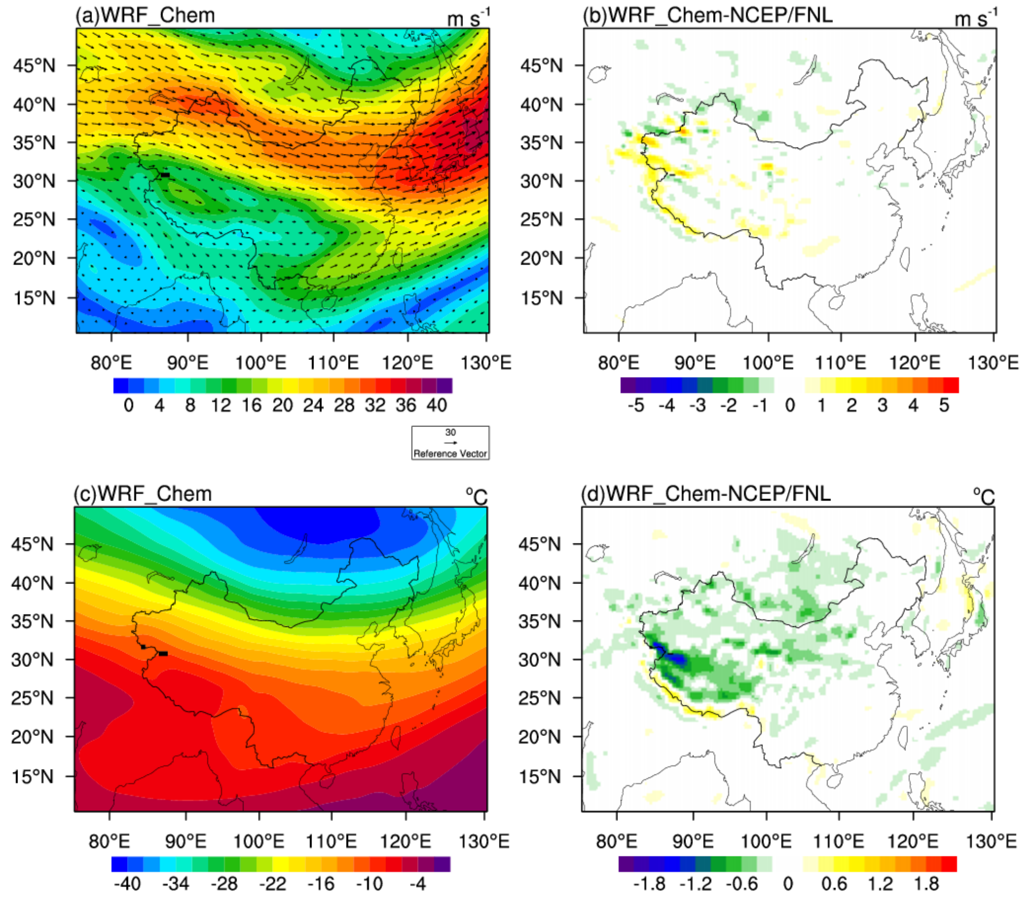

Fig.2 The simulated average wind (Fig. 2a) as well as temperature fields (Fig. 2c) at 500 hPa and the difference between the simulation and NCEP/FNL reanalysis data (Fig. 2b and Fig. 2d) over East Asia during March 18th to 23rd , 2010 (hereafter referred to the simulation period). Arrows represent wind vector at 500 hPa.

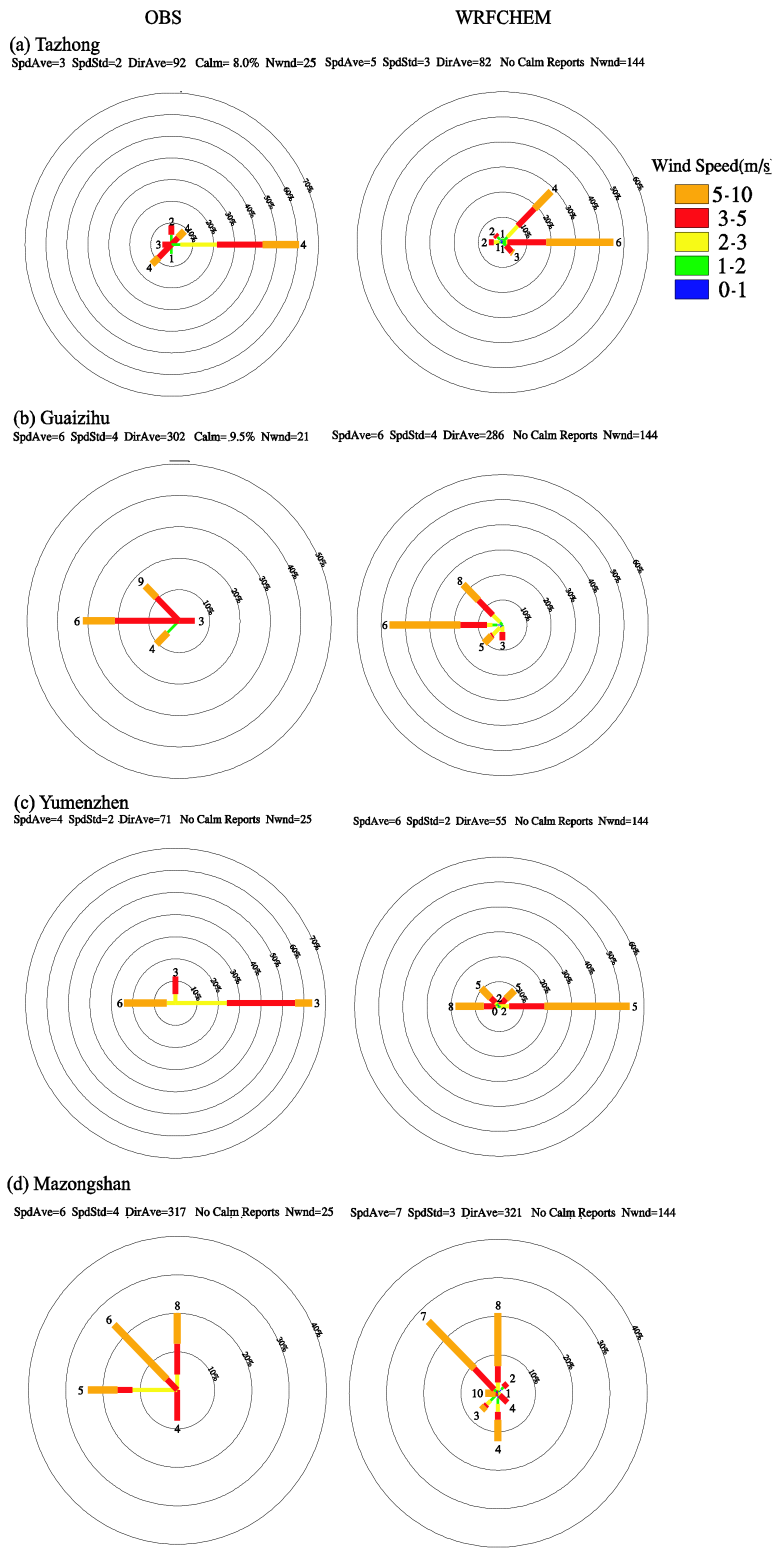

Fig. 3 Wind rose diagrams at the four meteorological stations: Tazhong (a), Guaizihu (b), Yumenzhen (c), and Maoyinbadao (d) over the TD and GD during the simulation period from observations and WRF-Chem model. The mean wind speed is included at the end of each directional line.

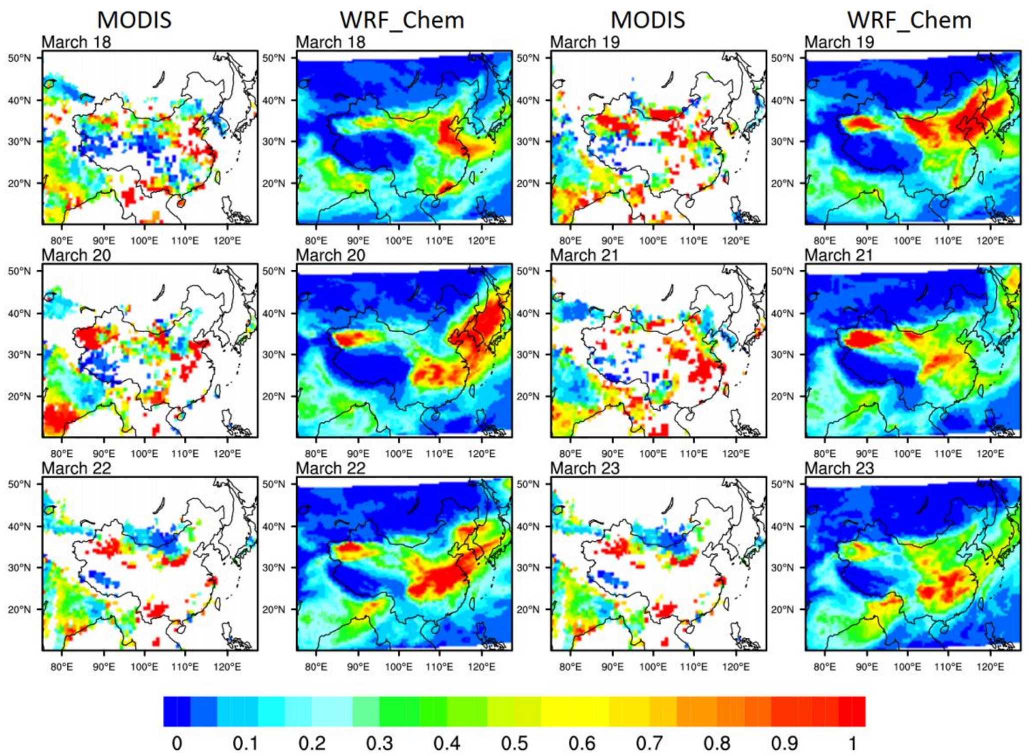

Fig. 4 Spatial distributions of the daily mean 550-nm aerosol optical depths from the MODIS retrievals and the corresponding WRF-Chem simulations over East Asia during the simulation period.

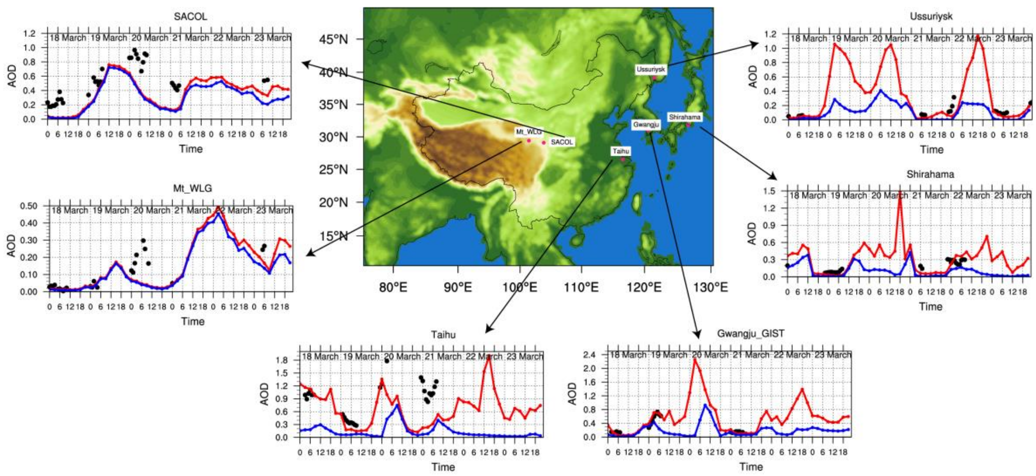

Fig. 5 Elevation map in the WRF-Chem domain and time series of the observed and modelled AOD at the six AERONET sites (SACOL, Taihu, Mt_Waliguan (Mt_WLG), Ussuriysk, Gwangju GIST, and Shirahama) during the simulation period. The black dots denote the 1 h averages of the observed AODs. The red and blue lines represent the modelled total and dust AODs from the WRF-Chem model, respectively.

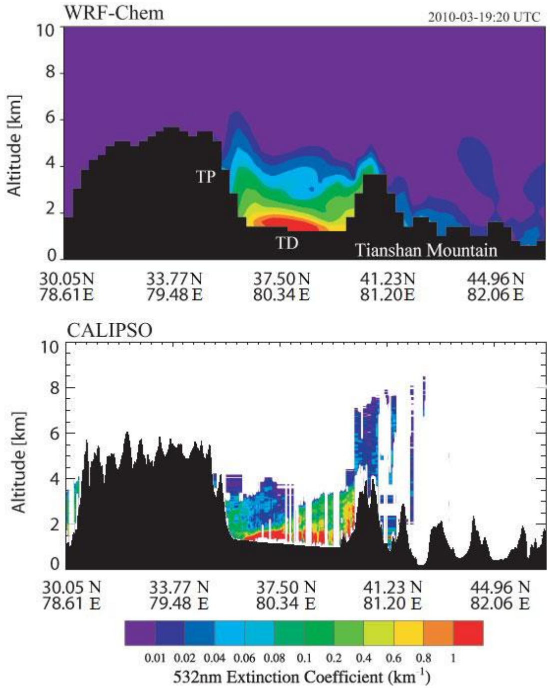

Fig. 6 Cross-sections of aerosol extinction coefficients at 532 nm (km^{-1}) over the TD at 20:08 UTC (2:08 LT) on 19th March 2010 from the WRF-Chem model (top) and CALIPSO retrievals (bottom) along the orbit path of CALIPSO (as shown in Fig. 1a).

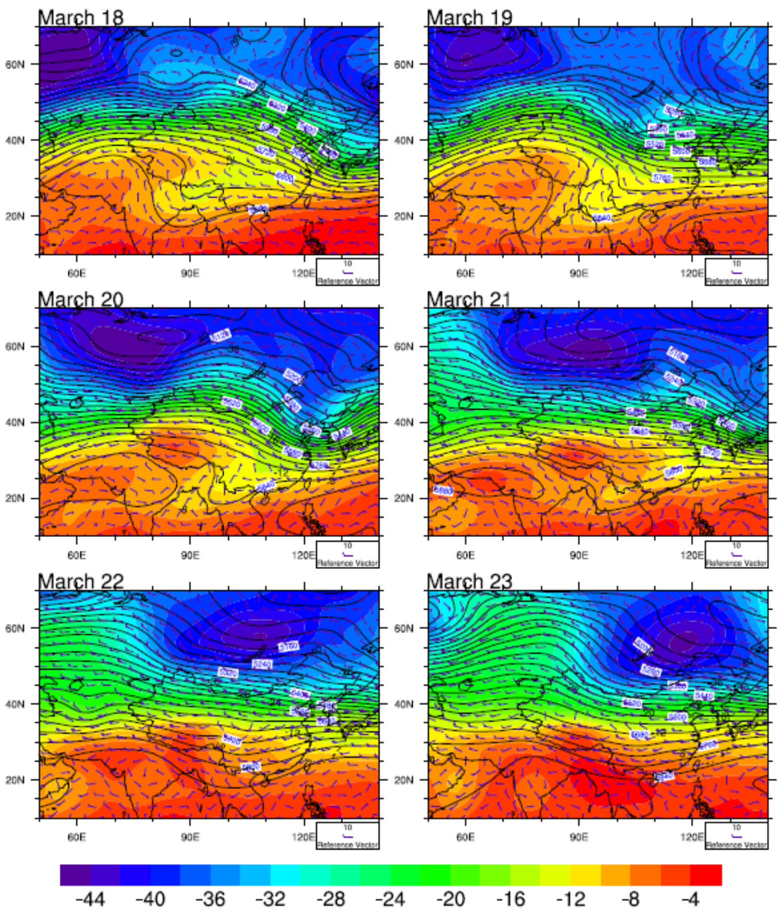

Fig. 7 Spatial distributions of geopotential heights (blue lines, unit: gpm), temperatures (color, unit: °C) at 500 hPa from the NCEP/FNL reanalysis data over East Asia during the simulation period. The vectors represent the wind field at 500 hPa (m s^{-1}).

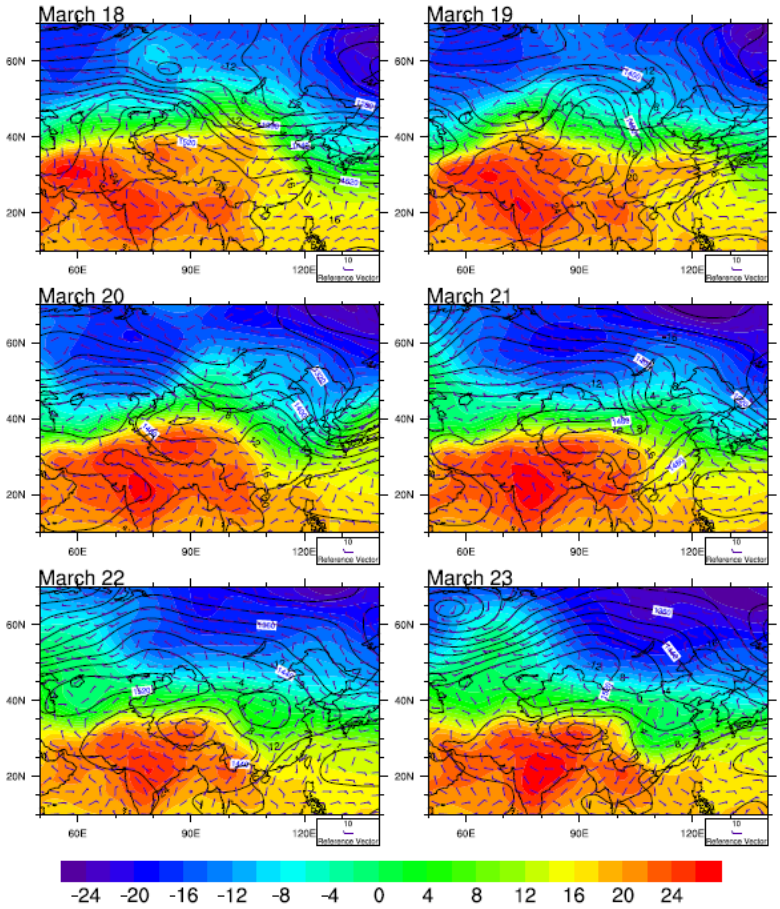

Fig.8 Spatial distributions of geopotential heights (blue lines, unit: gpm), temperatures (color, unit: °C) at 850 hPa from the NCEP/FNL reanalysis data over East Asia during the simulation period. The vectors represent the wind field at 850 hPa (m s^{-1}).

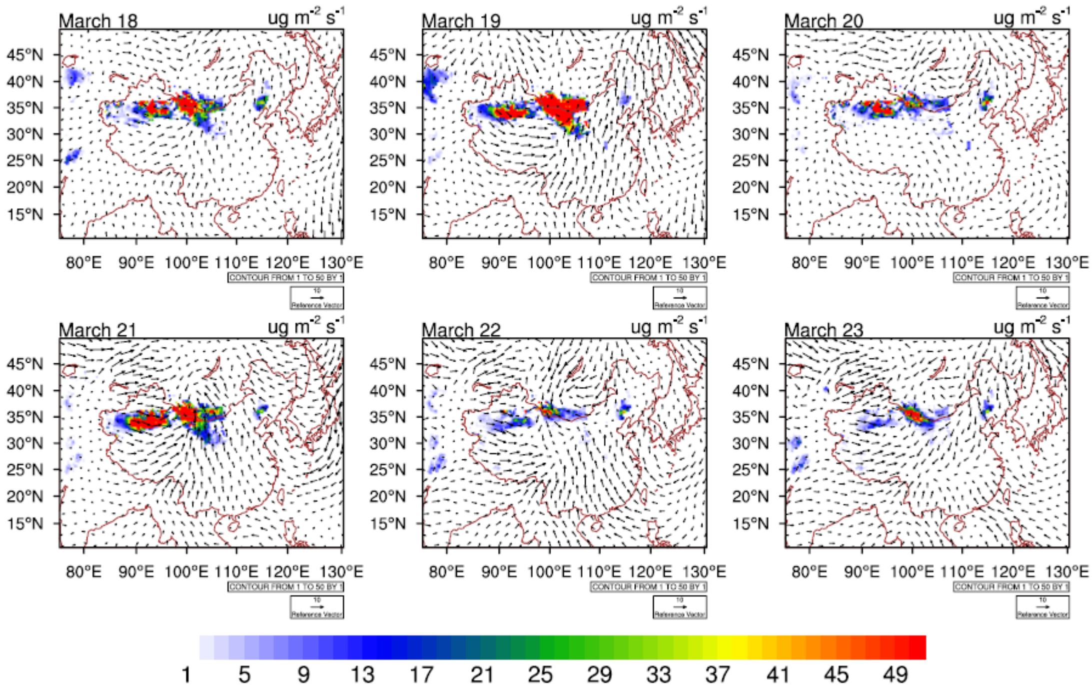

Fig. 9 Spatial distributions of daily dust emission (μg m^{-2} s^{-1}) over East Asia during the simulation period from WRF-Chem simulations. The arrows represent the wind vectors at 10 m (m s^{-1}).

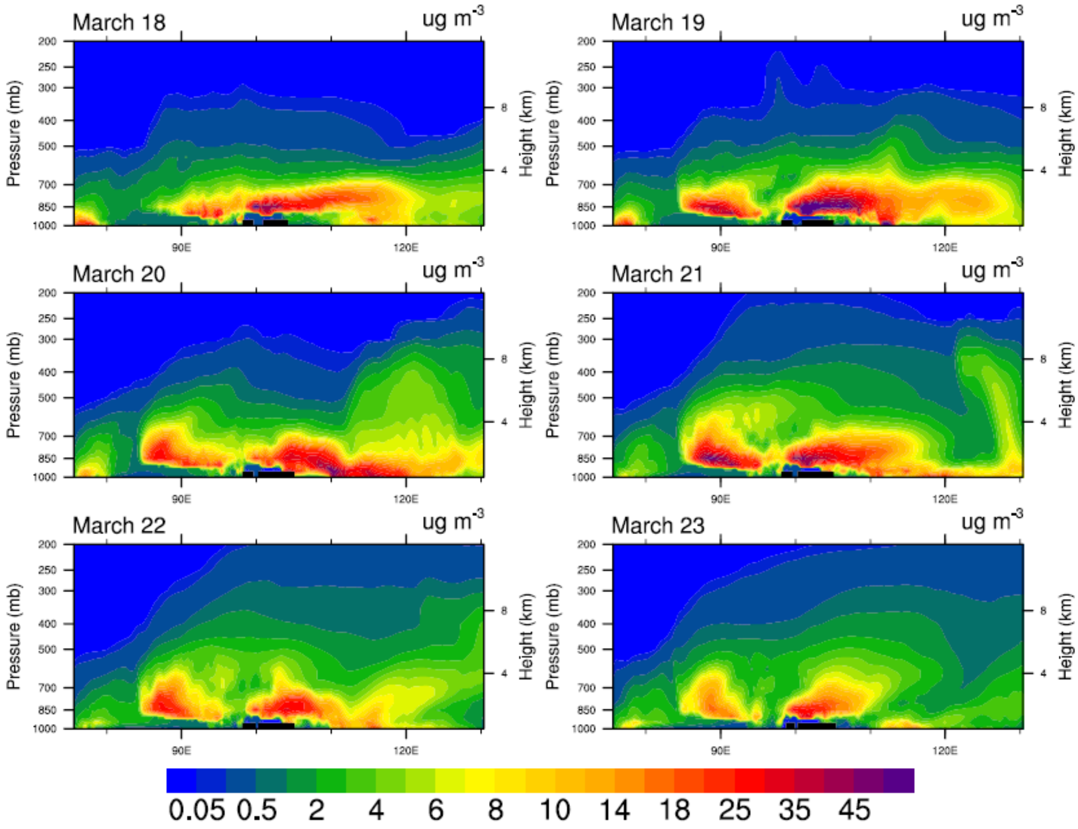

Fig. 10 Temporal and spatial cross sections of the meridional mean $PM_{2.5}$ dust concentration (ug m^{-3}) in the domain simulated by the WRF-Chem model during the simulation period.

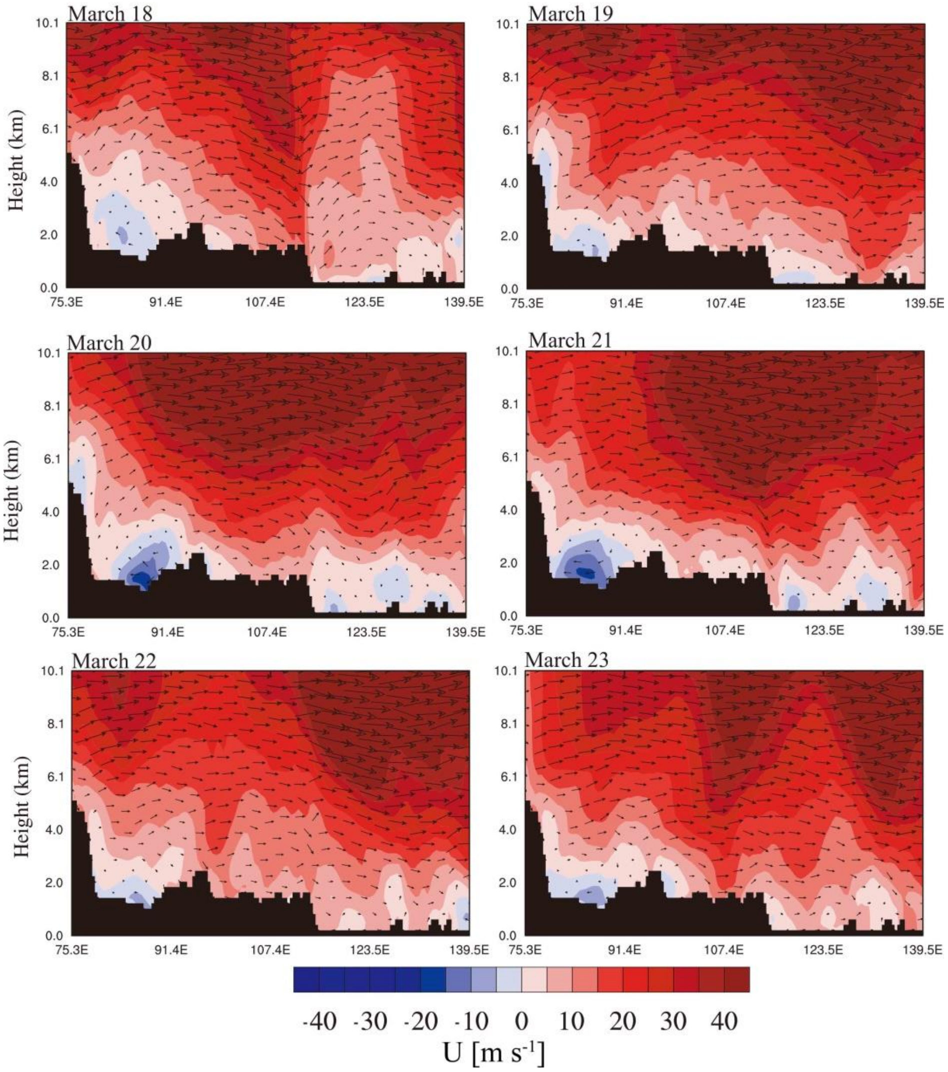

Fig. 11 Vertical-latitude cross section of zonal wind (m s^{-1}) and wind vector (the vertical wind scaled by 10^2) along 42°N during the simulation period from WRF-Chem simulation.

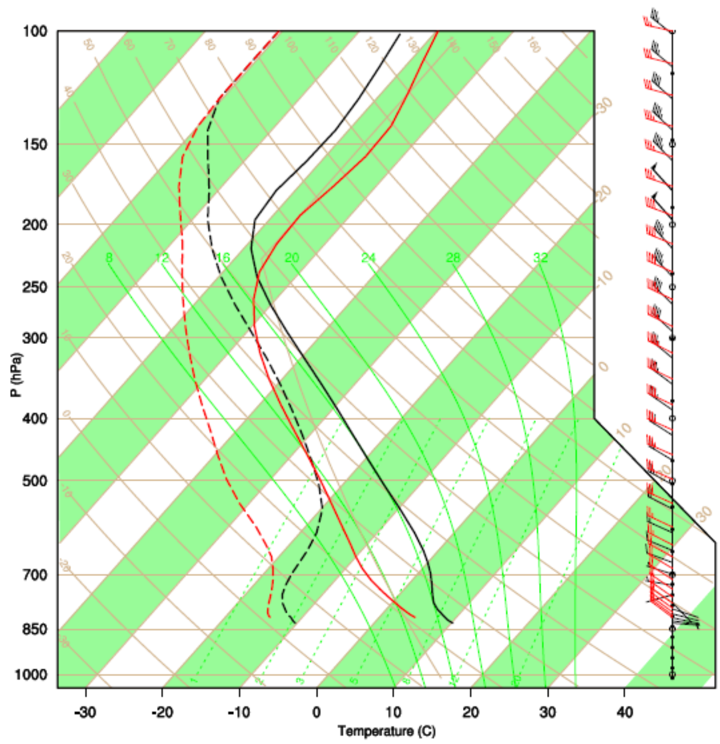

Fig.12 The skew T-log diagram over the TD (black lines) and GD (Red lines) on 19th March 2010 from the WRF-Chem simulation. The solid lines represent temperature and dash lines represent dew point temperature.

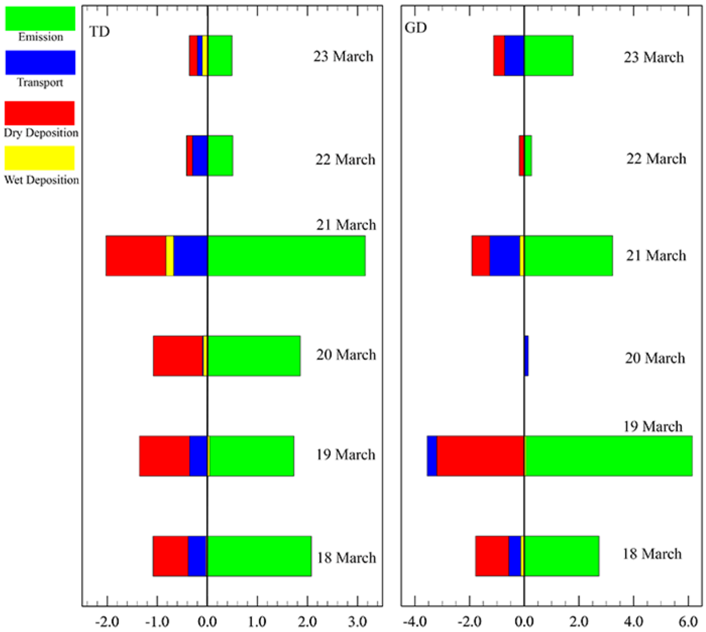

Fig. 13 Average contributions of the dust emissions, transport, and dry and wet depositions to the dust mass balances over the TD and GD during the simulation period based on the WRF-Chem model. The positive sign represents increase to dust concentration and the negative sign represents decrease to dust concentration. Units: tons day^{-1}.

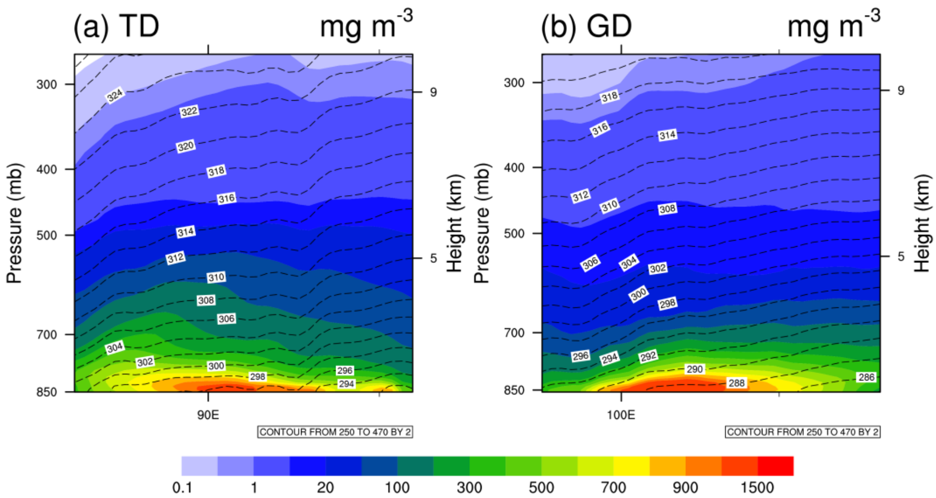

Fig. 14 Cross sections of the average dust mass concentrations (mg m^{-3}) over the TD (Fig. 14a) and GD (Fig. 14b) during the simulation period based on the WRF-Chem model. The black lines represent potential temperature (K).

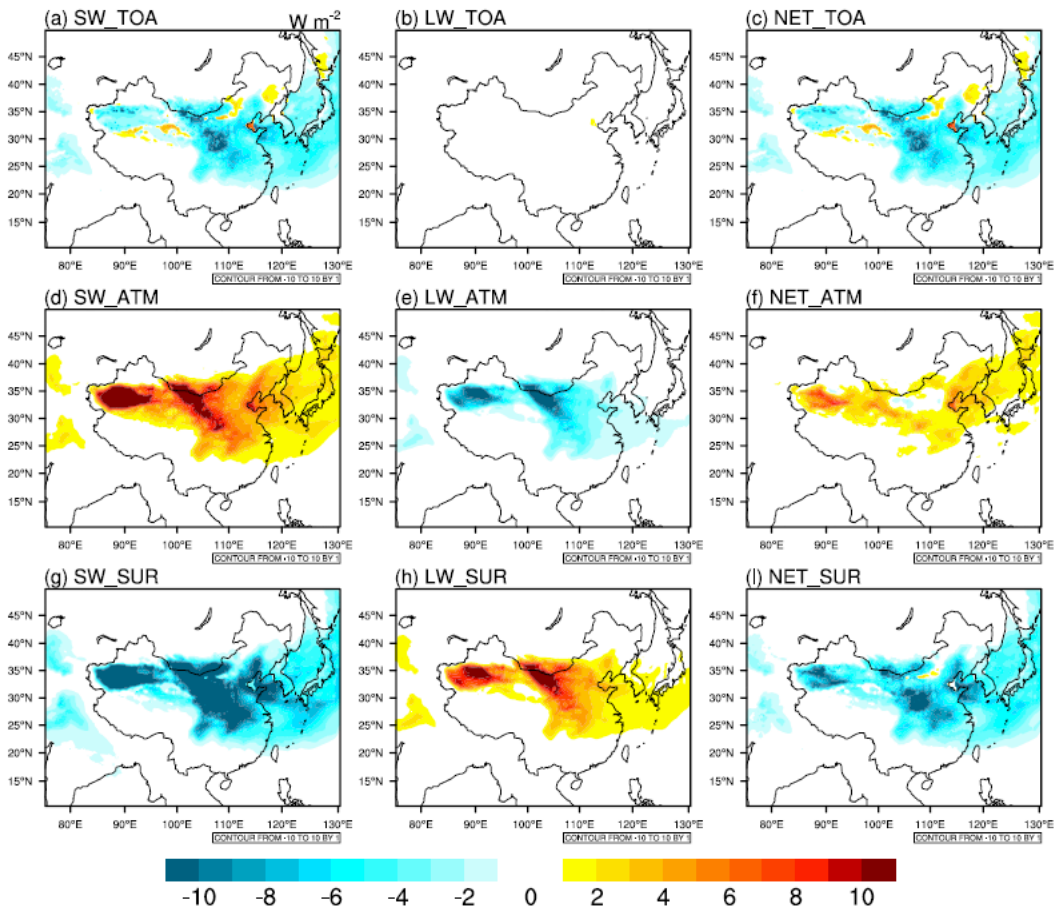

Fig. 15 Spatial distributions of dust direct radiative forcing for SW, LW, and net (SW+LW) radiation (W m^{-2}) at the TOA (top panels), SUR (bottom panels), and in the ATM (middle panels) average during the simulation period at all-sky conditions based on the WRF-Chem model. For dust direct radiative forcing, positive values at the TOA and SUR represent downward radiative fluxes, and represent radiative warming in the ATM.

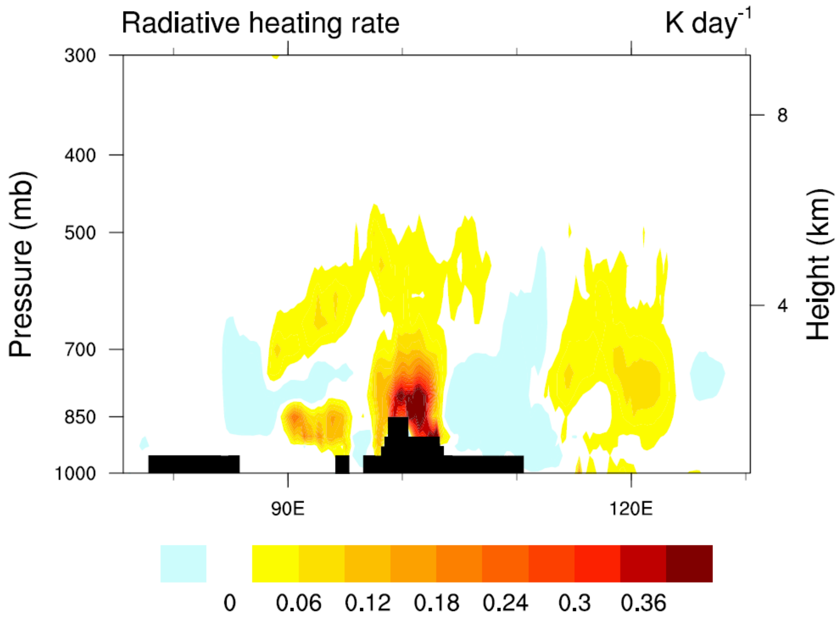

Fig. 16 Cross section of dust-induced radiative heating rate (K day^{-1}) from 15 °N to 45 °N during the simulation period from WRF-Chem simulation.